The Effect of Electronic Properties of Anodized and Hard Anodized Ti and Ti6Al4V on Their Reactivity in Simulated Body Fluid

The effect of electronic properties of anodized and hard anodized Ti and Ti6Al4V on their reactivity in Simulated Body Fluid

F. Di Franco[a], A. Zaffora[a,z], D. Pupillo[b], L. Iannucci[b], S. Grassini[b], M. Santamaria[a]

[a] Dipartimento di Ingegneria, Università degli Studi di Palermo, Viale delle Scienze, Ed. 6, 90128 Palermo, Italy

[b] Dipartimento di Scienza Applicata e Tecnologia, Politecnico di Torino, Corso Duca degli Abruzzi 24, 10129 Torino, Italy

[z]Corresponding author: andrea.zaffora@unipa.it

Authors e-mails:
francesco.difranco@unipa.it
davide.pupillo@polito.it
leonardo.iannucci@polito.it
sabrina.grassini@polito.it
monica.santamaria@unipa.it

Abstract

The electronic properties of barrier and porous layers on Ti and Ti6Al4V were studied. Barrier anodic oxides grown to 40 V on Ti and on Ti6Al4V are both n-type semiconductors with a band gap of 3.3 eV and 3.4 eV respectively, in agreement with the formation of amorphous TiO_2. Anodizing to 200 V at 20 mA cm^{-2} in calcium acetate and β-glycerol phosphate disodium pentahydrate leads to the formation of Ca and P containing porous films with a photoelectrochemical behaviour dependent on the metallic substrate. A band gap of 3.2 eV and the flat band potential of -0.5 V vs. Ag/AgCl were measured for the porous oxide on Ti, while optical transitions at 2.15 eV and a significantly more positive flat band potential were revealed for the porous oxide on the alloy. The different electronic properties were rationalized by taking into account the presence of localized states inside the gap, induced by incorporation of Al and V from the underlaying alloy during the hard anodizing process. These electronic properties are responsible of the reactivity of porous layer grown on Ti6Al4V alloy in simulated body fluid.

Keywords: Passive films; Ti alloys; Anodizing; Corrosion resistance; Simulated body fluid; Photoelectrochemistry

1 - Introduction

Titanium and its alloys are widely used in several technological applications, e.g. aerospace engineering [1,2] and biomedicine [3,4], due to their peculiar mechanical and physico-chemical properties in addition to a high corrosion resistance. Indeed, they are characterized by the spontaneous formation, as soon as they come in contact with oxygen, of a thin passive film whose composition is essentially titanium oxide. This passive film is very efficient, blocking both generalized and localized corrosion phenomena. Therefore, the loss of passivity of Ti and its alloys in body fluid environments and/or tissue systems is very difficult, unless the passive film is damaged by fretting/erosion action. However, in the case of biomedical applications, the high corrosion resistance of Ti and its alloys can significantly hinder the reactivity (bioactivity) of these materials with surrounding human body environment, making them bioinert hampering the chemical connection between materials and bones [5–8].

It is well known that the presence of hydroxyapatite (HA) improves the biocompatibility and thus the osteointegration of Ti alloys. The growth of HA on the surface of Ti and its alloys is promoted by a local alkalinization according to the following reaction [9]:

$$10Ca^{2+} + 8OH^- + 6HPO_4^{2-} \rightarrow Ca_{10}(PO_4)_6(OH)_2 + 6H_2O \quad (1)$$

A decrease in O_2 reduction or H_2 evolution reaction rates should slow down HA growth because of a decrease in OH^- concentration (see eq. (1)), thus passive films properties have a strong impact on the bio-inertness of Ti and Ti alloys. The blocking behaviour of the passive film toward electrochemical processes strongly depends on its solid state properties. In the case of Ti and Ti alloys such passive film is usually an amorphous TiO_2 layer with n-type semiconducting properties, i.e. blocking toward electrochemical reactions if positively polarized with respect to its flat band potential (reverse bias) and not blocking if negatively polarized with respect to its flat band potential (forward bias) [10,11]. Some authors focused their work on the study of semiconducting properties of thin passive/native oxides by using Mott-Schottky approach [12–14]. Nevertheless, to have information about the electronic properties of (thin and/or thick anodic) layers, photocurrent spectroscopy (PCS) is a more suitable technique, since it is able to provide information about the energetics of passive film/electrolyte interface (flat band potential estimate, valence and conduction band edges energy levels) and, indirectly (through the band gap values), about the chemical composition of anodic oxides[15].

As reported in literature, in order to improve the bioactivity of Ti and Ti alloys, and thus the HA growth, a possible strategy is to grow a thick porous anodic layer on the metal surface, using an electrolyte consisting of calcium acetate and β-glycerophosphate disodium salt pentahydrate [16–19].

Anodizing of Ti and Ti alloys has been widely studied on special interest on anodic layers composition and microstructure [17,20–22], but there is no information about electronic properties of such films. Since it sounds counterintuitive that the presence of thick ceramic material on the metal surface improves the bioactivity, in this work we want to study the electronic properties of TiO_2 layers grown by anodizing or hard anodizing on Ti and Ti6Al4V alloys with the aim to understand how they affect the corrosion resistance and thus the reactivity of these materials. Porous layers were grown in calcium acetate (CA, $(CH_3COO)_2Ca \cdot H_2O$) and β-glycerol phosphate disodium pentahydrate (β-GPDS) aqueous solution at room temperature (25 ± 2 °C) up to formation voltages of 200 V while barrier layers were grown to 40 V in phosphoric acid aqueous solution. Photoelectrochemical measurements were carried out to study the effect of the anodizing conditions and alloying elements (namely Al and V) on the optical band gap and flat band potential of the investigated oxide layers. Polarization curves were recorded in Simulated Body Fluid at 37°C in order to evaluate the reactivity of the samples as function of metal composition and anodizing conditions.

2 – Materials and methods

Materials

Titanium foils (Aldrich, purity > 99.7 %) with a dimension of 45 × 10 mm^2 and a thickness of 0.127 mm were etched in a mixture of hydrofluoric acid (39.5 %), nitric acid (69.0 %) and deionized water (1:4:5 vol.) for 30 seconds then ultrasonically cleaned in deionized water for 10 minutes. Samples were used immediately after being dried in air.

Ti6Al4V (Goodfellow) titanium alloy with a dimension of 45 × 20 mm^2 and a thickness of 2 mm was used. The samples were mechanically polished using SiC abrasive papers with P800, P1200 and P2400 grit. Subsequently, the samples were degreased using acetone in an ultrasonic bath and then were rinsed with deionized water.

Barrier and porous oxide layer growth

A two-electrode configuration was used, where the metal (Ti6Al4V alloys or Ti) was the anode (working electrode) and a Pt net having a very high specific area the cathode (counter electrode).

Growth of the barrier-type anodic film was carried out in 0.1 M H_3PO_4 aqueous solution [21,23]. Anodizing was performed galvanostatically at 5 mA cm^{-2}, reaching the final voltage (i.e. formation voltage) of 40 V. Then, a stabilization process was carried out keeping the final voltage for 30 min.

To grow porous oxide layers, Ti6Al4V alloys and Ti were anodized in an aqueous solution 0.2 M in calcium acetate (CA, $(CH_3COO)_2Ca \cdot H_2O$) and 0.04 M in β-glycerol phosphate disodium

pentahydrate (β-GPDS, $C_3H_7Na_2O_6P \cdot 5H_2O$). Anodic oxide growth was carried out galvanostatically at 20 mA cm^{-2} and the voltage compliance was set to 200 V.

SEM and XRD analysis

Samples morphology was investigated with a FEI Quanta 200 FEG SEM microscope coupled with Energy-Dispersive X-ray Spectrum (EDAX Genesis XM 4) facility. SEM operated in High Vacuum mode with a voltage of 20 kV. The software used to fit EDX spectra is EDX Genesis. Each sample was covered with a thin Au film deposited by sputtering before any investigation. X-ray diffraction (XRD) measurements were performed using a Pan Analytical Empyrean diffractometer with a Cu anode (Cu Kα radiation, $\lambda = 0.15405$ nm) equipped with PIXCel1D detector (voltage: 40 kV, current: 40 mA). The XRD patterns were collected over the 2θ angle range: 10° - 90°.

Photoelectrochemical characterization

The experimental setup used for the photoelectrochemical investigations consists of a 450 W UV–VIS xenon lamp coupled with a monochromator (Kratos), which allows monochromatic irradiation of the specimen surface through the photoelectrochemical cell quartz windows. The cell volume for the photoelectrochemical measurements was 50 mL. A two-phase lock-in amplifier (EG&G) was used in connection with a mechanical chopper (frequency: 13 Hz) to separate the photocurrent from the total current circulating in the cell due to the potentiostatic control. Photocurrent spectra reported below are corrected for the relative photon flux of the light source at each wavelength, so that the photocurrent yield in arbitrary current units is represented in the y axis. The samples were characterized in 0.1 M ABE ($(NH_4)_2B_4O_7 \cdot 4\ H_2O$, pH ~ 8.5) aqueous solution.

The experiments were conducted at least on three different samples with an uncertainty on the band gap value of ± 0.05 eV. This is a type B uncertainty since is due to the monochromator resolution that is in the order of ± 3 nm.

All the experiments were performed in air at room temperature (25 ± 2 °C). For all the experiments, a Pt net having a very high surface area was used as counter electrode and a silver/silver chloride electrode (SSC) was employed as reference electrode for all photoelectrochemical experiments.

Polarization Curves

Polarization curves were recorded using a Parstat 2263 (PAR), with a scan rate of 2 $mV \cdot s^{-1}$. The three-electrode configuration was the same used for the photoelectrochemical experiments. The cell volume of the electrochemical cell was 100 mL. The samples were characterized in Simulated Body Fluid solution (see composition in Table 1) at 37°C. OCP (Open Circuit Potential) was recorded for

at least 1 hour and then a polarization curve was recorded starting to sweep the electrode potential toward anodic direction from -150 mV vs OCP. E_{corr} and i_{corr} were estimated by using Tafel Extrapolation Method.

Results and discussion

Air formed passive film

Fig. 1 shows photocurrent spectra recorded at open circuit potential relating to the air formed passive films grown on Ti and Ti6Al4V.

Assuming indirect optical transitions, it is possible to estimate the band gap values according to the following equation:

$$(Q_{ph}\ h\nu)^{0.5} \sim (h\nu - E_g) \qquad (2)$$

where, for photon energy in the vicinity of band gap, Q_{ph}, the photocurrent yield, is proportional to the light absorption coefficient, $h\nu$ is the photon energy and E_g is the optical band gap [24,25]. E_g = 3.76 eV is estimated for air formed film on Ti while an E_g = 3.62 eV is estimated for air formed film on Ti6Al4V. These values are higher than optical band gap reported for anatase (i.e. 3.20 eV) and rutile (i.e. 3.05 eV) TiO_2 polymorphs, and it is usually attributed to the formation of a not crystalline and/or defective titanium oxide. Indeed, a not perfect stoichiometry and/or the lack of long range order can induce the formation of localized states close to the band edges [26]. In this case optical band gap is more properly called mobility gap [27]. Current vs time curves, recorded at the open circuit potential by manually chopping monochromatic irradiation for air formed films grown on Ti and Ti6Al4V, are shown in Fig. S1. In both cases the measured photocurrent is anodic as expected for n-type semiconductors but, notably, a lower I_{ph} was measured for the oxide grown on the alloy.

Barrier oxide layer growth

In Fig. 2 the cell voltage vs time curves recorded during the anodizing process in phosphoric acid solution on Ti and Ti6Al4V alloys are reported. In both cases the voltage raises linearly up to the compliance of 40 V (maintained for 30 min to allow the formation of a less defective film) in agreement with the formation of a barrier anodic oxide.

According to the high field mechanism [28,29], the slope of the V vs time curve, dV/dt, is given by the following equation:

$$\frac{dV}{dt} = \eta \frac{iXM}{zF\rho} \quad (3)$$

where i is the current density (kept constant in this case during the anodizing process), M is the molecular weight of the growing oxide, z the number of electrons circulating per mole of formed oxide, F the Faraday constant, ρ the film density, X is the electric field strength across the growing layer and η is the growth efficiency. For both Ti and Ti6Al4V alloys a dV/dt of ~ 1.6 V s^{-1} is estimated. Assuming the formation of TiO_2 as anodic film on both samples, from eq. (3), with ρ_{TiO2} = 3.7 g cm^{-3} [30], X = 5.7 MV cm^{-1} can be estimated, corresponding to an anodizing ratio (i.e. the reciprocal of the electric field strength) of ~ 17 Å V^{-1} [20]. Thus, assuming an equilibrium potential for Ti oxidation to TiO_2 of ~ -1.2 V vs SHE [31], formation voltages of 40 V (vs. cathode) correspond to anodic layer thickness of ~ 70 nm. This barrier layer thickness has been estimated considering the anodizing ratio derived from eq. (3), that is valid for valve metals and assuming a unitary growth efficiency. The estimated anodizing ratio is in agreement with other values reported in the literature [20], and published TEM pictures of anodic film cross sections[21] confirm this estimate. It is also noteworthy to mention that, during anodizing of Ti and Ti alloys, cations (produced by metal oxidation) migrate toward the oxide/electrolyte interface while oxygen ions produced by water deprotonation migrate toward the metal/oxide interface with other anions present in the electrolyte (namely phosphate). Thus, the latter are concentrated in the outer part of the film.

In order to estimate the optical band gap of oxide layers, photocurrent spectra (photocurrent vs irradiating wavelength curves) were recorded in 0.1 M ABE at 2 V vs Ag/AgCl (see Fig. 3a and Fig.3b).

By assuming non direct optical transitions, an E_g = 3.30 eV is estimated for anodic film on Ti (see inset Fig. 3a) in agreement with previous results reported in the literature for not crystalline or defective titanium oxide [23]. In the case of anodic film grown on Ti6Al4V, a band gap of ~ 3.40 eV is estimated (see inset Fig. 3b), slightly higher with respect to that estimated for anodic film on Ti, suggesting an even lower crystalline character. The following is the primary cause of the differences between the photocurrent response of less crystalline/amorphous and crystalline thin films: the presence of various types of defects might change the DOS distribution, thus the optical band gap of an amorphous material may coincide or not with that of its crystalline counterpart. This is also confirmed by the lower photocurrent measured for the anodic film on the alloy. In fact in less crystalline/amorphous anodic oxide, the presence of geminate recombination effect involving generated photocarriers, can reduce the recorded photocurrent signal[15].

Figure S2 shows the current vs time curves recorded at 2 V vs. Ag/AgCl by manually chopping monochromatic irradiation for 40 V anodic films grown on Ti and Ti6Al4V. In both cases the

measured photocurrent is anodic as expected for n-type semiconductors but, notably, a lower I_{ph} was measured for the oxide grown on the alloy.

In Figure 4 the I_{ph} vs potential curves recorded at different wavelengths are reported. I_{ph} decreases shifting the potential toward the negative (i.e. cathodic) direction, as expected for n-type semiconducting materials.

Zero photocurrent potential can provide an estimate of the flat band potential (E_{FB}) of the oxides, which is in turn linked to the oxide Fermi level, E_{ox}^{F}, according to the following relationship [25]:

$$E_{ox}^{F} = -|e|E_{FB} + |e|E_{ref} \quad (4)$$

where *e* is the electron charge and E_{ref} is the potential of the reference electrode (Ag/AgCl) with respect to the vacuum scale. For anodic films on Ti and Ti6Al4V E_{FB} are ~ -0.5 V vs Ag/AgCl and -0.6 V vs Ag/AgCl, respectively. The latter is slightly more negative suggesting that the Fermi level of anodic film on the alloy is closer to the conduction band edge than for the anodic film on Ti.

The photocharacteristics were fitted (see Figures S3) according to the following power law:

$$I_{ph}^{n} \propto E \quad (5)$$

The best fitting exponent n was 1.7 for the anodic film on Ti for both the irradiating wavelengths (see Table 2). According to Gärtner-Butler model, valid for crystalline SC/electrolyte junction, the dependence of photocurrent on electrode potential should be quadratic, and n slightly lower than 2 can be explained by the lack of long range order in the thin amorphous TiO_2 and a consequent lower mobility of the photogenerated charge [32]. In the case of the photocharacteristics recorded for the anodic layer grown on Ti6Al4V alloy (see Figure 4b), the best fitting exponent n is 1, i.e. photocurrent has a linear dependency on electrode potential indicating an even lower mobility of the photogenerated carriers in localized states.

During anodizing Ti, Al and V have very similar transport number, thus they are incorporated from the base alloy into the anodic layer roughly proportionally to their percentage in the alloy. According to the experimental photoelectrochemical findings, such incorporation phenomena do not significantly affect the electronic properties of the barrier layers.

Porous oxide layer growth

Fig. 5 shows the growth curve (cell voltage vs. time) for Ti and Ti6Al4V anodized in CA and β-GPDS-containing solution at 20 mA cm^{-2}.

A linear dependence of cell potential on time is observed during the early stages of the anodizing process, as typical of the growth of barrier anodic oxide, i.e. compact and uniform oxide film [30]. For cell potential higher than ~ 50 V, oxygen evolution reaction occurs with a change in the slope of the growth curve, decreasing the efficiency of the whole anodizing process. Higher cell potential leads to the dielectric breakdown on the oxide film causing the formation of an outer porous structure in a hard anodizing regime, as also demonstrated by the oscillations in the growth curve for cell potential values higher than ~ 165 V. Under hard anodizing conditions the imposed electric field is so high that the film breaks and repairs continuously and the results is a porous oxide whose composition depends not only on the employed electrolyte but also on the metallic substrate composition [33]. Under these anodizing conditions, porous layer thickness is estimated to be ~2.5 μm, according to what reported by Ishizawa and Ogino[17].

Fig. 6 shows SEM micrographs of Ti and Ti6Al4V after anodizing to 200 V, disclosing a multiscale porous structure with a wide distribution of pores diameter. In contrast with previous results reported in the literature for anodic layers grown in more concentrated CA and β-GPDS-containing solutions [19], the oxide is cracks free. EDX analysis (reported in Table 3) reveals that the anodic layers contain Ti and O, but also Ca and P. For films grown on Ti6Al4V, EDX analysis (reported in Table 3) reveals also the presence of Al and V incorporated into the oxide during the anodizing process [22].

Figure 7 shows the X ray diffraction patterns recorded for Ti and Ti6Al4V after anodizing to 200 V. Apart from the reflections of the substrates (namely bare Ti and Ti6Al4V), reflections (101) and (200) of anatase, corresponding to $2\theta = 25.3°$ and 48.05° respectively (see inset of Figure 7a), are present for the anodic oxides grown on Ti, suggesting the formation of this TiO_2 polymorph [10]. For the anodic oxide grown on Ti6Al4V, only reflection (101) is present (see inset of Figure 7b) and, even, less intense suggesting a lower crystallinity degree.

Photocurrent spectra recorded in 0.1 M ABE for Ti and Ti6Al4V after anodizing to 200 V are reported in Figure 8. They show two main differences: the photocurrent is lower for the anodic oxide grown on the alloy with respect to that measured for the anodic oxide grown on Ti; the light absorption threshold of the anodic film on Ti6Al4V is shifted toward low photon energy with respect to the oxide on Ti. The optical band gap, estimated according to eq. (2), is 3.20 eV for 200 V anodic film on Ti, thus coincident with the value reported in the literature for anatase [10], in agreement with the XRD pattern. A significantly lower value (i.e. 2.15 eV) was estimated for 200 V anodic film on Ti6Al4V (see inset of Figure 8).

For both films the photocurrent is anodic, as confirmed by the current transients reported in Fig. S4. Notably, for the oxide grown on Ti6Al4V, stationary anodic photocurrent was measured under 420 nm irradiation (see Fig. 8c).

Other relevant experimental findings arise from the photocharacteristics (see Figure 9). The shape of the photocharacteristics is completely different depending on the metallic substrate. In fact, photocurrent vs electrode potential curves for anodic oxide grown on Ti to 200 V (see Figure 9a) can be fitted according to eq. (5) with an exponent n close to 2 (see fitting in Figures S5), due to the higher crystalline degree with respect to the corresponding oxide grown to 40 V. Photocharacteristics for anodic layer grown on Ti6Al4V alloy (see Figure 9b) can be fitted with eq. (5) (see fitting in Figures S5) with exponent n much lower than 1 (supralinear curves), indicating the occurrence of strong recombination phenomena (see Table 2). Moreover, zero photocurrent potential for 200 V anodic film on Ti6Al4V (0.5 V vs. Ag/AgCl) is significantly more positive than that measured for 40 V barrier film thus shifting E_{ox}^{F} toward mid gap according to eq. (4). This is not the case of 200 V anodic oxide on Ti, whose zero photocurrent potential (-0.5 V vs. Ag/AgCl) is close to that measured for the 40 V barrier layer.

The photoelectrochemical findings can be explained by the changes in the electronic properties of the oxide induced by incorporation of Al^{3+} and V^{5+} ions during the anodizing process of Ti6Al4V causing a doping of the titanium oxide. Anodic TiO_2 is a n-type semiconductor due to its self-doping, since it is usually substoichiometric (TiO_{2-x}) and thus donor levels are usually present close to the conduction band due to oxygen vacancies (i.e. Ti^{3+}). Al^{3+} ions incorporated into TiO_2 matrix behave like Ti^{3+} leading to the formation of oxygen vacancies (donor states close to the conduction band). Conversely, the presence of V^{5+} ions into TiO_2 crystalline matrix can cause the formation of acceptor states (close to the valence band) inside the mobility gap (see scheme of Figure 10), responsible for the shift of E_{FB} toward more positive values. These doping mechanisms, due to the incorporation of Al^{3+} and V^{5+} ions into TiO_2 matrix, can be also expressed according to the Kröger–Vink notation[11,34]:

$$Al_2O_3 \xrightarrow{TiO_2} 2\,Al'_{Ti} + 3\,O_O^x + V_O^{\cdot\cdot} \qquad (6)$$

$$V_2O_5 \xrightarrow{TiO_2} 2\,V_{Ti}^{\cdot} + 5\,O_O^x + \frac{1}{2}\,V_{Ti}^{''''} \qquad (7)$$

Moreover, these states can be responsible for optical transitions under photon energies lower than TiO_2 band gap explaining the lower absorption threshold. And since these states are localized, the mobility of photogenerated charges is very low explaining the low best fitting exponent n found for the photocharacteristics. This does not imply a change in conduction band edge energy level, that is

reported to happen when a mixed oxide is prepared with two or more cations present in comparable concentration [35].

Characterization in Simulated Body Fluid

Fig. 11 shows polarization curves recorded at 2 mV s^{-1} in Simulated Body Fluid at 37°C. For all samples the cathodic branch of the polarization curves is related to the oxygen reduction reaction. In the case of the bare samples the current in the anodic branch is due to passivation of the metals while for the anodized samples, it is due the re-passivation reactions occurring in the oxide.

In Table 4 E_{corr} and i_{corr} estimated from polarization curves are reported. For both Ti and Ti6Al4V, barrier type anodic oxide shows the lowest corrosion current density. In the case of porous type anodic oxides, i_{corr} value (~10^{-2} μA/cm^2) estimated for the oxide grown on Ti is lower with respect to i_{corr} estimated for bare sample (~5×10^{-2} μA/cm^2). For the oxides grown on Ti alloy, i_{corr} estimated for the porous type anodic oxide and for bare sample are almost equal (~6×10^{-2} μA/cm^2) and higher with respect to that estimated for porous type anodic layer grown on Ti. This result is directly related to the electronic properties of the anodic oxides. In fact, in the case of 200 V oxide grown on Ti, E_{corr} (~ -0.27 V vs. Ag/AgCl, see Table 4) is more anodic than flat band potential estimated from the photocharacteristic curve (~ -0.5 V vs. Ag/AgCl). The anodic layer is polarized in reverse bias regime and, therefore, the oxide behaves as insulating material, hindering oxidation and/or reduction reactions.

In the case of 200 V oxide grown on Ti6Al4V, E_{corr} (~ 0.01 V vs. Ag/AgCl, see Table 4) is more cathodic than flat band potential estimated from the photocharacteristic curve (~ 0.5 V vs. Ag/AgCl), therefore the anodic layer is polarized in forward bias regime leading to a less blocking behaviour toward oxidation/reduction reactions. Moreover, according to the photoelectrochemical characterization, 200 V anodic oxide grown on Ti6Al4V alloy has localized electronic states inside the mobility gap that can increase the electronic conduction through the anodic layer.

The less blocking character of the porous anodic oxide grown on Ti6Al4V alloy leads to oxygen reduction reaction, that occurs in a confined environment (the pore of the anodic layer) inducing a local alkalinization. This, together with the release of Ca^{2+} ions incorporated into the oxide during the anodizing process, leads to the growth of HA (see eq. 1), improving the bioactivity of the TAV alloy. It is noteworthy to mention that the growth of a thick anodic layer hinders the release of V ions into the human body environment [22].

Conclusions

Here we studied the electronic properties of TiO_2 layers grown by anodizing or hard anodizing on Ti and Ti6Al4V alloys with the aim to understand how they affect the corrosion resistance and thus the reactivity of these materials in simulated body fluid environment. Ti and Ti6Al4V alloy were anodized at 5 mA cm^{-2} to 40 V in 0.1 M H_3PO_4 to induce the formation of barrier type oxide and to compare their electronic properties. Photoelectrochemical characterization revealed that both barrier layers are n-type semiconductors with a band gap of 3.3 eV and 3.4 eV for anodic films on Ti and on Ti6Al4V respectively, thus slightly higher than that reported for crystalline TiO_2 in agreement with the formation of amorphous oxides. The flat band potential of the barrier anodic films on Ti and Ti6Al4V are close to each other, with a slightly more negative value measured for the oxide grown on the alloy.

Ti and Ti6Al4V alloy were also anodized to 200 V at 20 mA cm^{-2} in calcium acetate and β-glycerol phosphate disodium pentahydrate aqueous solution to induce the formation of porous oxide, as confirmed by SEM micrographs. EDX analysis revealed that calcium and phosphorus are incorporated during the anodizing process. Notably, porous layers on Ti6Al4V also contain Al and V incorporated from the underlaying alloy. According to photoelectrochemical characterization, a band gap of 3.2 eV is estimated for porous film on Ti, thus coincident with that reported for anatase (in agreement with the reflections in the corresponding XRD pattern), and with a flat band potential very close to that estimated for the barrier layer. Conversely, optical transitions at energy significantly lower (2.15 eV) were recorded for the porous film on Ti6Al4V, that can be explained by incorporation of Al^{3+} and V^{5+} ions into TiO_2 matrix during the hard anodizing process. The incorporation of such aliovalent ions with respect to Ti^{4+} induces the formation of allowed localized states inside the gap of TiO_2 and accounts for the relevant shift toward more positive value of the oxide flat band potential.

This strong change of the electronic properties of the porous oxide on Ti6Al4V can explain the comparable (or even higher) corrosion current density in simulated body fluid of the alloy after hard anodizing to 200 V with respect to bare and 40 V anodized Ti6Al4V. Therefore, the hard anodizing process does not compromise the reactivity of the alloy in biological environment.

References

1. X. Zhang, Y. Chen, and J. Hu, *Prog. Aerosp. Sci.*, **97**, 22–34 (2018).

2. J. C. Williams and R. R. Boyer, *Metals (Basel).*, **10**, 705 (2020).

3. L. C. Zhang and L. Y. Chen, *Adv. Eng. Mater.*, **21**, 1801215 (2019).

4. J. W. Nicholson, *Prosthesis*, **2**, 100–116 (2020).

5. G. He, L. Xie, G. F. Yin, X. M. Liao, Y. W. Zou, Z. B. Huang, Y. D. Yao, X. C. Chen, and F. H. Wang, *Surf. Coatings Technol.*, **228**, 201–208 (2013) http://dx.doi.org/10.1016/j.surfcoat.2013.04.030.

6. Y. Ni, Z. Liu, W. Gao, S. Qu, J. Weng, and B. Feng, *Appl. Surf. Sci.*, **257**, 9287–9292 (2011) http://dx.doi.org/10.1016/j.apsusc.2011.05.007.

7. H. J. Song, M. K. Kim, G. C. Jung, M. S. Vang, and Y. J. Park, *Surf. Coatings Technol.*, **201**, 8738–8745 (2007).

8. Y. J. Chen, B. Feng, Y. P. Zhu, J. Weng, J. X. Wang, and X. Lu, *Mater. Lett.*, **63**, 2659–2661 (2009) http://dx.doi.org/10.1016/j.matlet.2009.09.029.

9. V. T. Nguyen, T. C. Cheng, T. H. Fang, and M. H. Li, *J. Mater. Res. Technol.*, **9**, 4817–4825 (2020).

10. M. Santamaria, G. Conigliaro, F. Di Franco, B. Megna, and F. Di Quarto, *J. Electrochem. Soc.*, **164**, C113–C120 (2017).

11. N. Sato, *Electrochemistry at Metal and Semiconductor Electrodes*, Elsevier Science B.V., Amsterdam, (1998).

12. M. Shahsavari, A. Imani, R. F. Schaller, and E. Asselin, *J. Appl. Electrochem.*, **52**, 1003–1019 (2022) https://doi.org/10.1007/s10800-022-01683-0.

13. F. E. T. Heakal and O. S. Shehata, *Prot. Met. Phys. Chem. Surfaces*, **56**, 333–342 (2020).

14. D. Il Seo and J. B. Lee, *Corros. Sci.*, **173**, 108789 (2020) https://doi.org/10.1016/j.corsci.2020.108789.

15. F. Di Quarto, F. Di Franco, A. Zaffora, and M. Santamaria, in *Encyclopedia of Interfacial Chemistry: Surface Science and Electrochemistry*, K. Wandelt, Editor, vol. 1, p. 361–371, Elsevier Inc. (2018).

16. H. Ishizawa, M. Fujino, and M. Ogino, *J. Biomed. Mater. Res.*, **29**, 1459–1468 (1995).

17. H. Ishizawa and M. Ogino, *J. Biomed. Mater. Res.*, **29**, 65–72 (1995).

18. W. W. Son, X. Zhu, H. I. Shin, J. L. Ong, and K. H. Kim, *J. Biomed. Mater. Res. - Part B Appl. Biomater.*, **66**, 520–525 (2003).

19. A. C. Alves, F. Wenger, P. Ponthiaux, J. P. Celis, A. M. Pinto, L. A. Rocha, and J. C. S. Fernandes, *Electrochim. Acta*, **234**, 16–27 (2017).

20. H. Habazaki, K. Shimizu, S. Nagata, P. Skeldon, G. E. Thompson, and G. C. Wood, *Corros. Sci.*, **44**, 1047–1055 (2002).
21. H. Habazaki, M. Uozumi, H. Konno, K. Shimizu, P. Skeldon, and G. E. Thompson, *Corros. Sci.*, **45**, 2063–2073 (2003).
22. E. Matykina, M. Montuori, J. Gough, F. Monfort, A. Berkani, P. Skeldon, G. E. Thompson, and H. Habazaki, *Trans. Inst. Met. Finish.*, **84**, 125–133 (2006).
23. F. Di Quarto, F. Di Franco, C. Monarca, M. Santamaria, and H. Habazaki, *Electrochim. Acta*, **110**, 517–525 (2013).
24. A. Zaffora, M. Santamaria, F. Di Franco, H. Habazaki, and F. Di Quarto, *Electrochim. Acta*, **201**, 333–339 (2016).
25. A. Zaffora, F. Di Franco, F. Di Quarto, R. Macaluso, M. Mosca, H. Habazaki, and M. Santamaria, *ECS J. Solid State Sci. Technol.*, **6**, N25–N31 (2017).
26. N. F. Mott and E. A. Davis, *Electronic Processes In Non-Crystalline Materials*, 2nd ed., Clarendon Press, Oxford, U.K., (1979).
27. F. Di Franco, A. Zaffora, and M. Santamaria, *Electrochim. Acta*, **265**, 326–335 (2018).
28. M. M. Lohrengel, *Mater. Sci. Eng. R Reports*, **11**, 243–294 (1993).
29. A. Zaffora, G. Tranchida, F. Di Franco, F. Di Quarto, and M. Santamaria, *J. Electrochem. Soc.*, **163**, C563–C570 (2016).
30. M. T. Tanvir, K. Fushimi, K. Shimizu, S. Nagata, P. Skeldon, G. E. Thompson, and H. Habazaki, *Electrochim. Acta*, **52**, 6834–6840 (2007).
31. M. Pourbaix, *Atlas of electrochemical equilibria in aqueous solutions*, Pergamon Press, Oxford, UK, (1966).
32. A. Zaffora, M. Santamaria, F. Di Franco, H. Habazaki, and F. Di Quarto, *Phys. Chem. Chem. Phys.*, **18**, 351–360 (2016).
33. A. L. Yerokhin, X. Nie, A. Leyland, A. Matthews, and S. J. Dowey, *Surf. Coatings Technol.*, **122**, 73–93 (1999).
34. M. Epifani, R. Díaz, C. Force, E. Comini, T. Andreu, R. R. Zamani, J. Arbiol, P. Siciliano, G. Faglia, and J. R. Morante, *J. Phys. Chem. C*, **117**, 20697–20705 (2013).
35. M. Santamaria, F. Di Franco, F. Di Quarto, P. Skeldon, and G. E. Thompson, *J. Phys. Chem. C*, **117**, 4201–4210 (2013).

Figures

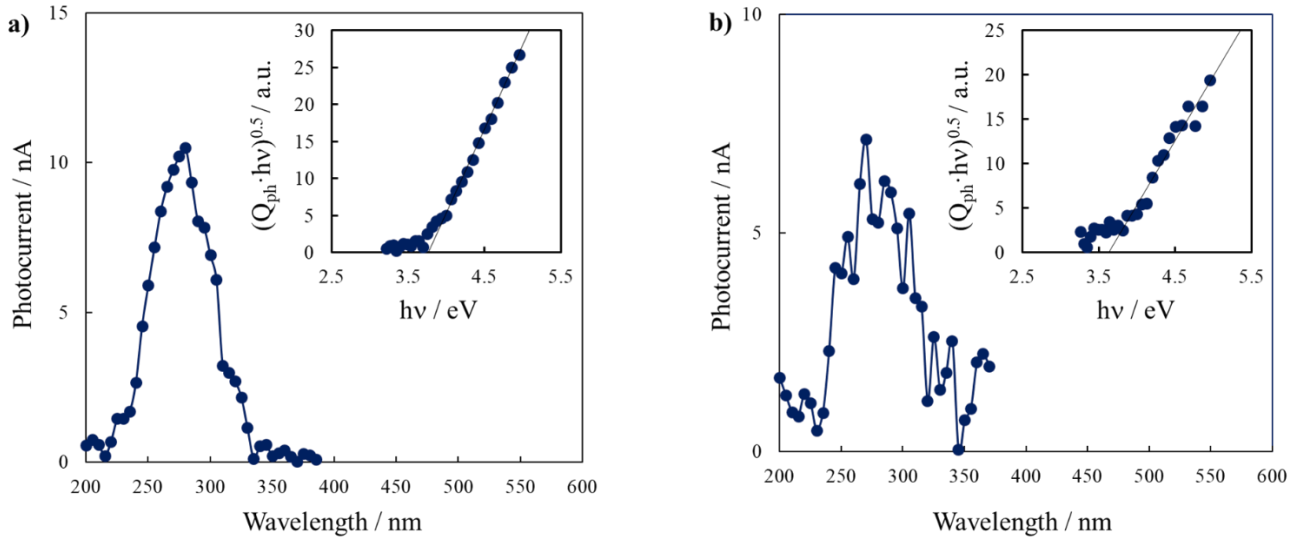

Figure 1. Photocurrent spectra recorded in 0.1 M ABE at OCP (~ - 0 V vs. Ag/AgCl and ~ - 0.2V vs. Ag/AgCl for Ti and Ti6Al4V respectively) for air formed film grown on a) Ti and b) Ti6Al4V alloy.

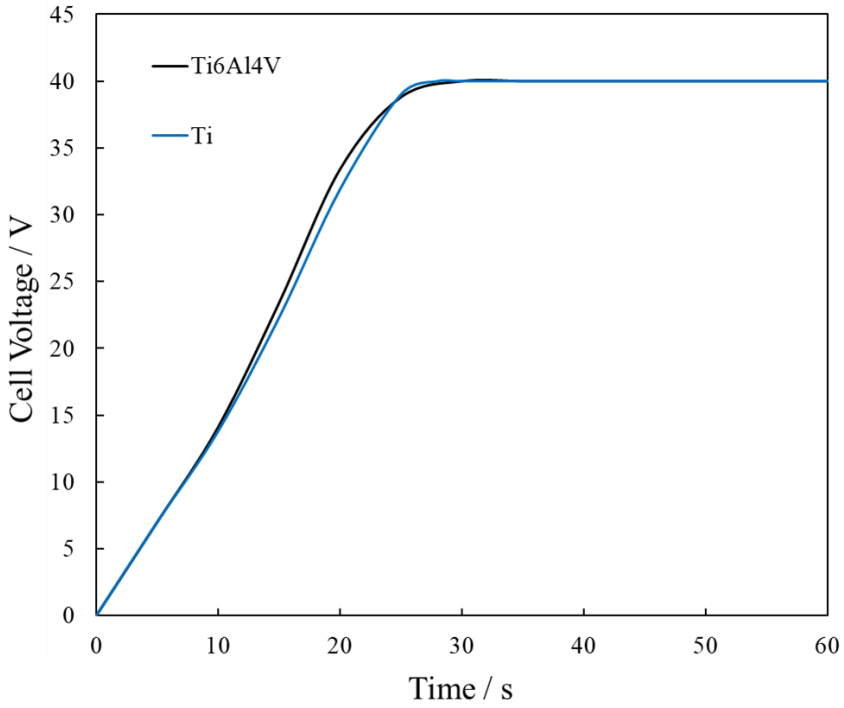

Figure 2. Growth curve of Ti and Ti6Al4V alloy in 0.1 M H_3PO_4, anodized galvanostatically at 5 mA cm^{-2}.

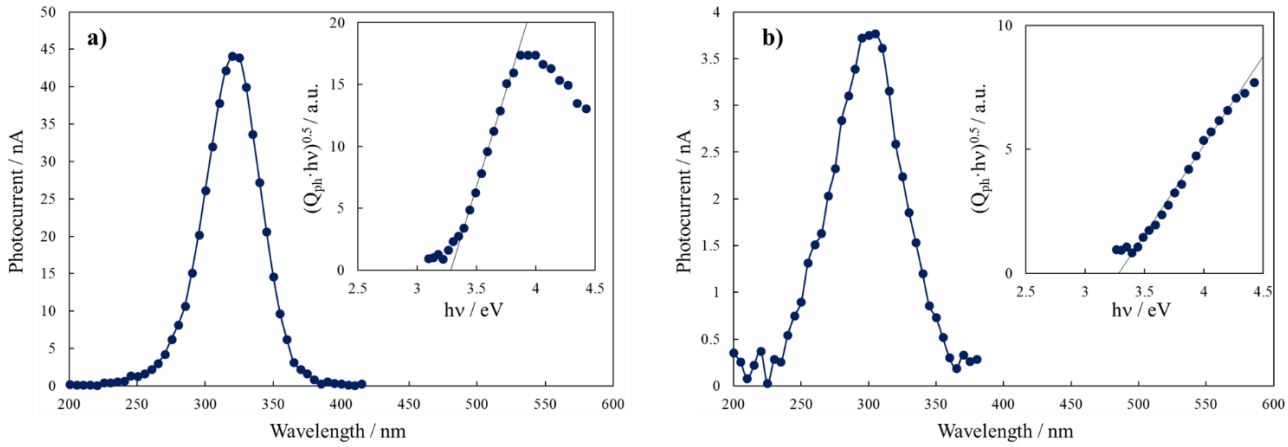

Figure 3. Photocurrent spectra recorded in 0.1 M ABE at 2 V vs Ag/AgCl for anodic oxides grown to 40 V on a) Ti and b) Ti6Al4V alloy.

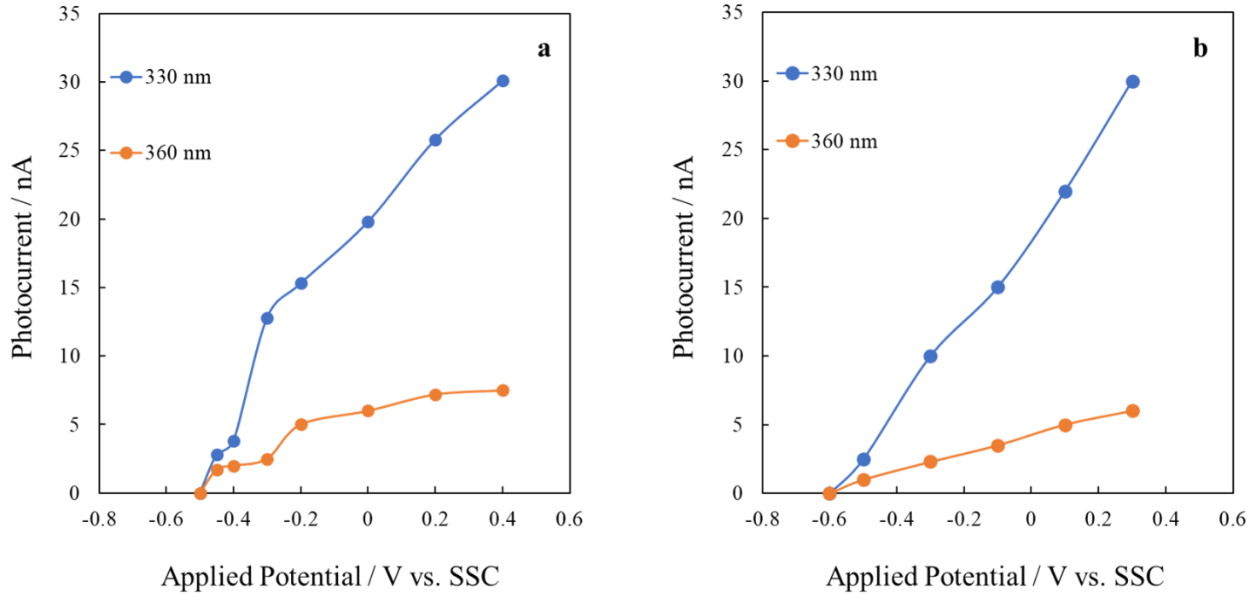

Figure 4. Photocharacteristics recorded in 0.1 M ABE at different wavelengths for anodic oxides grown to 40 V on a) Ti and b) Ti6Al4V alloy. The lines are drawn to guide the eyes, fitted photocharacteristics are reported in Fig. S3.

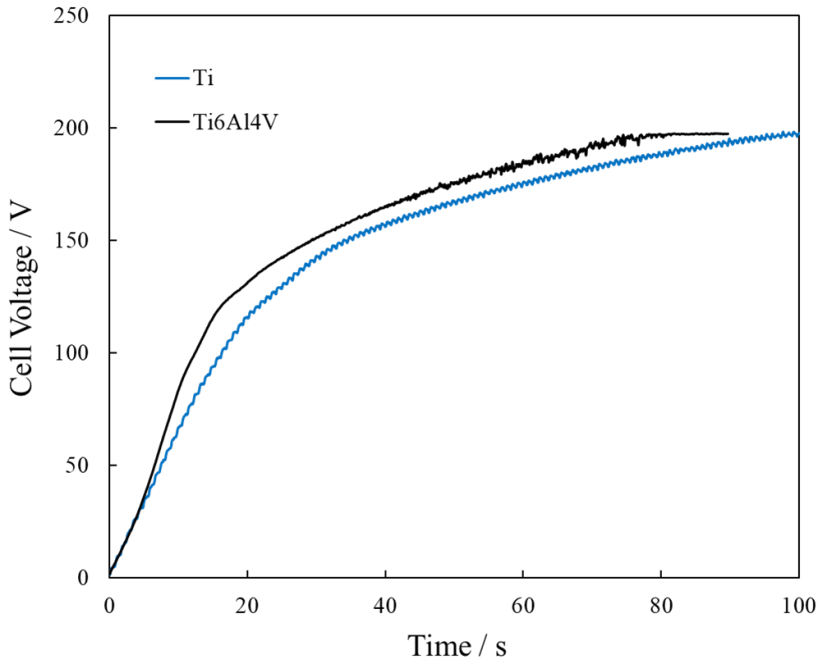

Figure 5. Growth curve of Ti and Ti6Al4V alloy in 0.2 M CA and 0.04 M β-GPDS, anodized galvanostatically at 20 mA cm^{-2}.

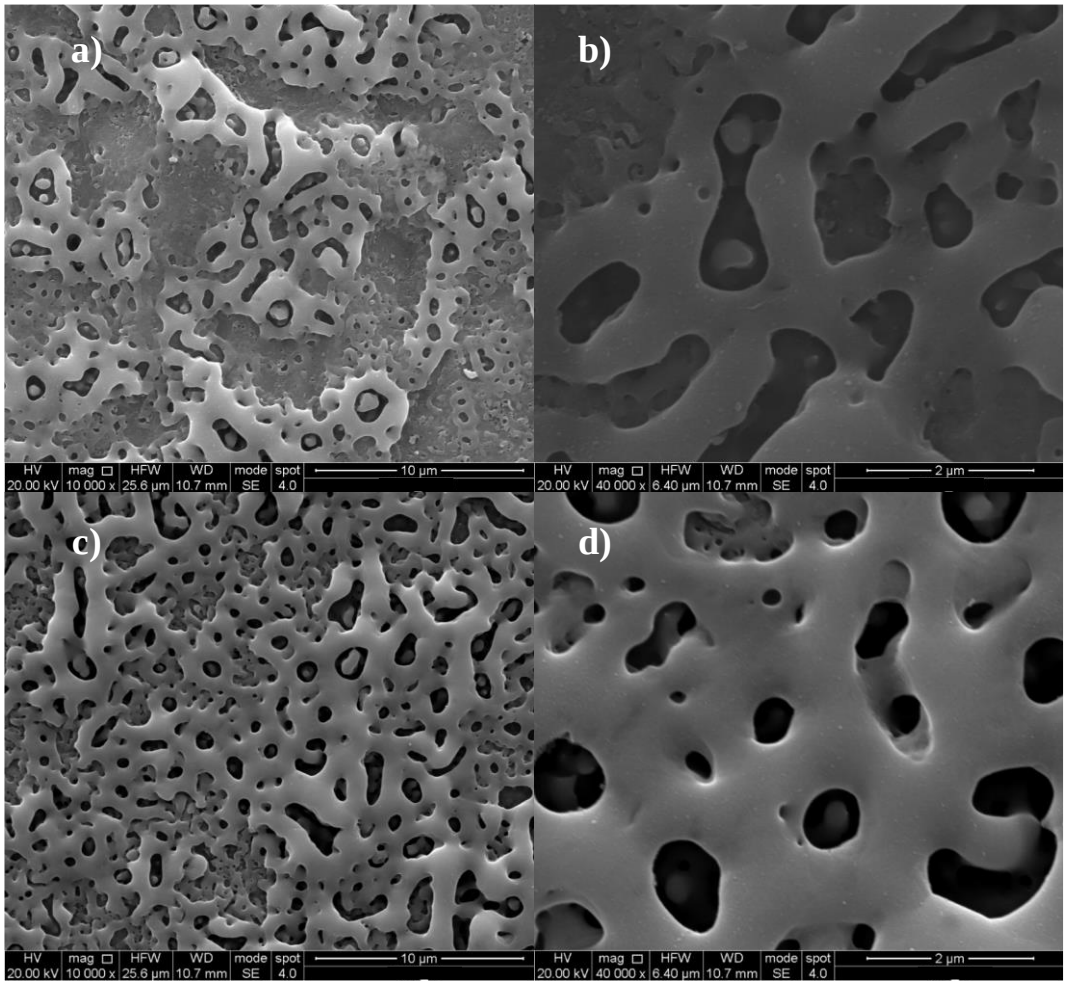

Figure 6. SEM micrographs of surface of anodic layers grown in 0.2 M CA and 0.04 M β-GPDS at 20 mA cm^{-2} to 200 V on a,b) Ti and c,d) Ti6Al4V alloy.

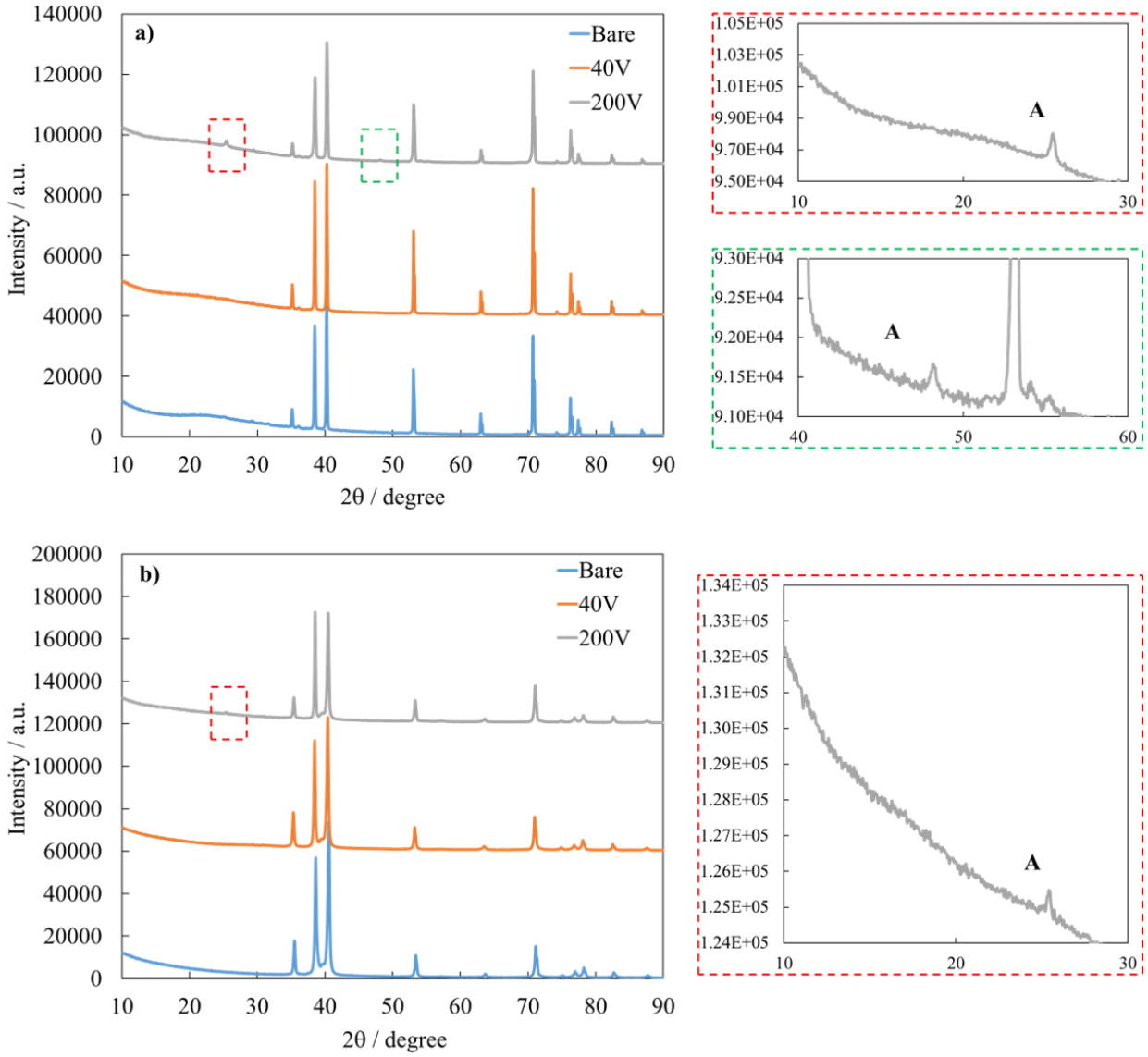

Figure 7. XRD patterns of anodic layers grown in 0.2 M CA and 0.04 M β-GPDS at 20 mA cm^{-2} to 200 V on a) Ti and b) Ti6Al4V alloy.

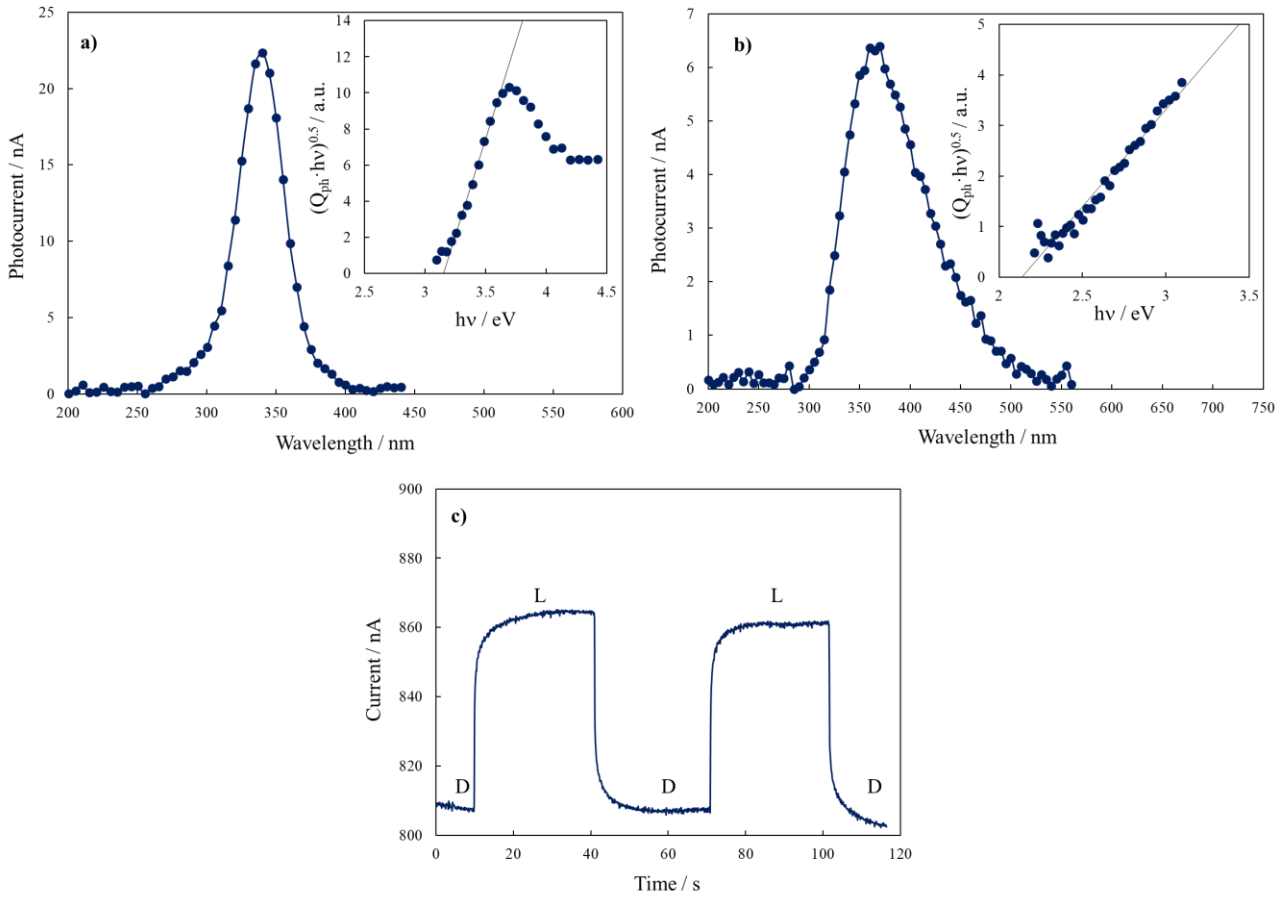

Figure 8. Photocurrent spectra recorded in 0.1 M ABE at 2 V vs Ag/AgCl for anodic oxides grown to 200 V on a) Ti and b) Ti6Al4V alloy. c) Current vs time curves recorded, by manually chopping the irradiation, under λ = 420 nm for anodic oxides grown to 200 V on Ti6Al4V alloy. L: light, D: dark.

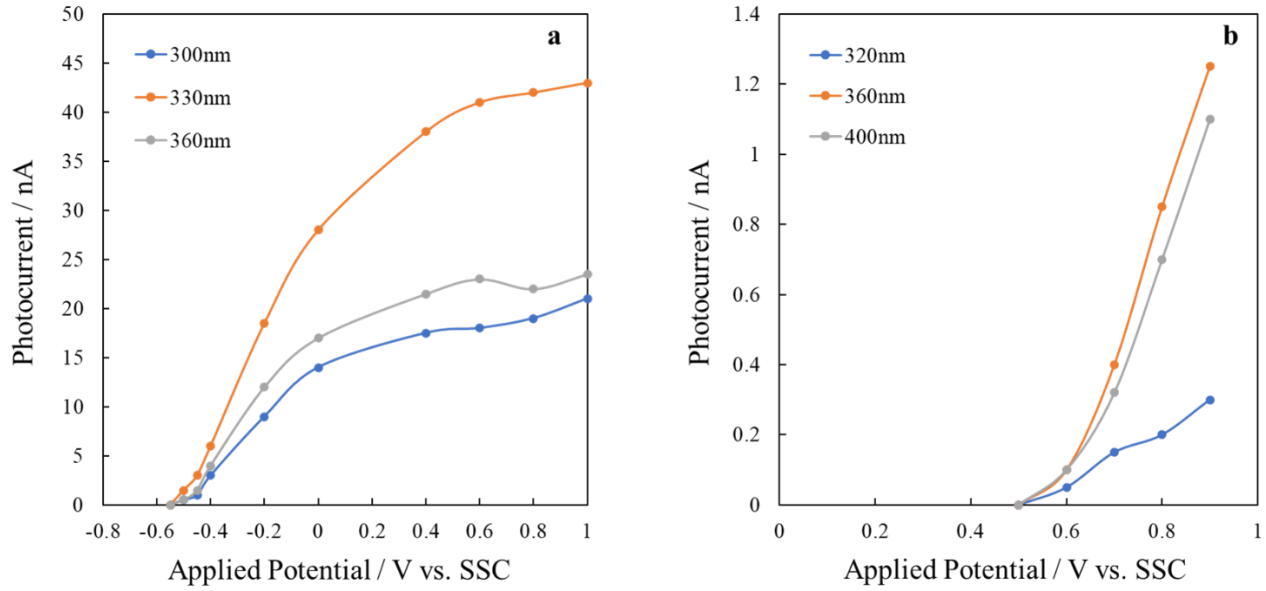

Figure 9. Photocharacteristics recorded in 0.1 M ABE at different wavelengths for anodic oxides grown to 200 V on a) Ti and b) Ti6Al4V alloy. The lines are drawn to guide the eyes, fitted photocharacteristics are given in Fig. S5.

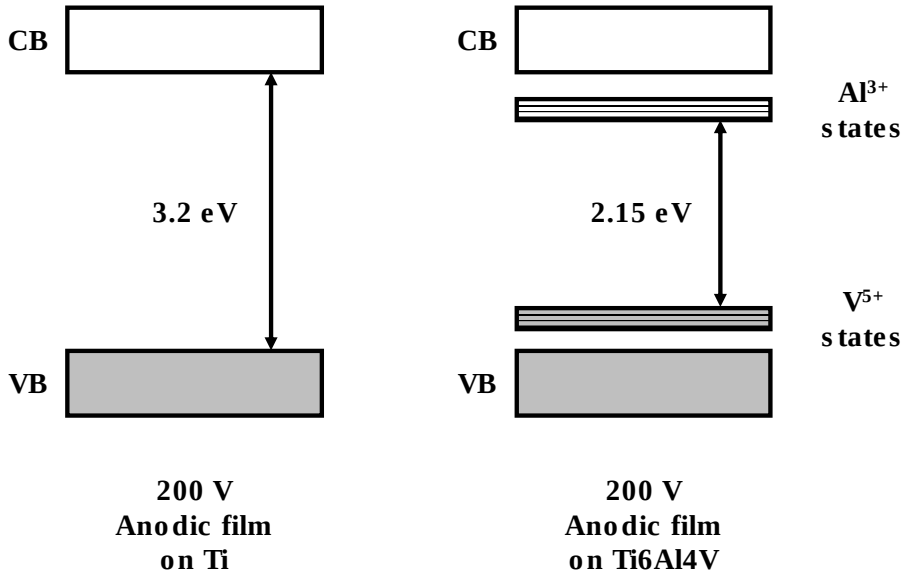

Figure 10. Scheme of band structure of 200 V anodic film grown on Ti and Ti6Al4V.

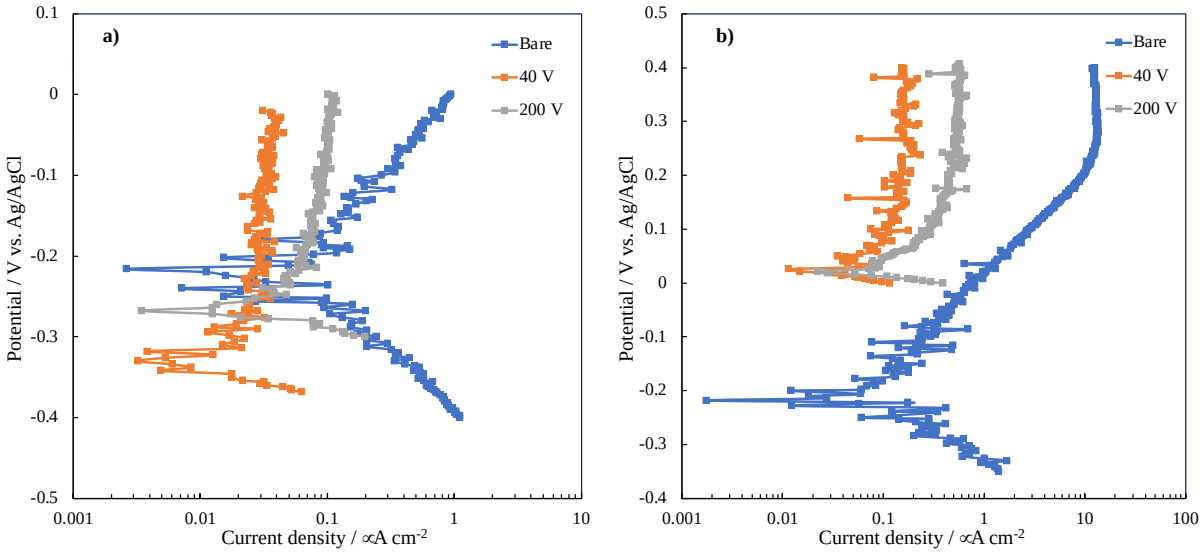

Figure 11. Polarization curves recorded in SBF for air formed and anodized samples on a) Ti and b) Ti6Al4V alloy.

Tables

Table 1. Composition of Hanks' solution (pH = 7.3).

Component	Concentration [g l^{-1}]
NaCl	8
KCl	0.4
$NaHCO_3$	0.35
$NaH_2PO_4 \cdot H_2O$	0.25
$Na_2HPO_4 \cdot H_2O$	0.06
$CaCl_2 \cdot 2H_2O$	0.19
$MgCl_2$	0.19
$MgSO_4 \cdot 7H_2O$	0.06
Glucose	1

Table 2. Comparison between the exponent n estimated from the best fitting according to Eq. (5) of the photocharacteristics relating to anodic films on Ti and Ti6Al4V alloy.

Sample	λ / nm	n
Ti 40 V	330	1.7
	360	1.7
Ti6Al4V 40 V	330	1
	360	1
Ti 200 V	300	2
	330	2
	360	2
Ti6Al4V 200 V	320	0.85
	360	0.5
	400	0.5

Table 3. Results from EDX analysis for anodic oxides grown on Ti and Ti6Al4V to 200 V.

	Ti		Ti6Al4V	
Element	**Wt %**	**At %**	**Wt %**	**At %**
O	29.5	55.1	32.6	57.1
Ti	67.4	42.1	54.1	31.7
Al	/	/	3.5	3.7

V	/	/	1.8	1
Ca	1.1	0.9	3.5	2.5
P	2	1.9	4.5	4

Table 4. E_{corr} and i_{corr} estimated from polarization curves of Figure 11.

Metal	**Sample**	**E_{corr} [V] vs. Ag/AgCl**	**i_{corr} [μA/cm^2]**
Ti	Bare	-0.22 ± 0.03	$(5 \pm 2) \times 10^{-2}$
	40 V	-0.34 ± 0.05	$(8 \pm 5) \times 10^{-3}$
	200 V	-0.27 ± 0.1	$(1 \pm 1) \times 10^{-2}$
Ti6Al4V	Bare	-0.20 ± 0.05	$(6 \pm 3) \times 10^{-2}$
	40 V	0.02 ± 0.08	$(3 \pm 2) \times 10^{-2}$
	200 V	0.01 ± 0.1	$(6 \pm 2) \times 10^{-2}$